Effect of Platinum Nanoparticle Loading on Oxygen Reduction at a Pt Nanocluster-Activated Microporous–Mesoporous Carbon Support

E. Härk · R. Jäger · E. Lust

Abstract Very high surface area carbon-supported Pt nanoparticle catalysts have been applied to the oxygen reduction reaction in alkaline solution. The distribution effect of deposited Pt nanoparticles onto the carbon support on the oxygen reduction reaction kinetics has been established by comparing the various carbon-supported Pt (20 and 60 wt% metal) catalysts. The various Pt catalysts were prepared by using a sodium borohydride reduction method. All the catalysts showed a face-centered cubic crystal structure as determined by X-ray diffraction method; the average platinum particle sizes were ~4.2, ~4.8, ~5.4, and ~27.2 nm for 20 wt% Pt–C(Mo$_2$C), 60 wt% Pt–C(Mo$_2$C)-I, 60 wt% Pt–Vulcan XC72, and 60 wt% Pt–C(Mo$_2$C)-II catalysts, respectively. The X-ray photoelectron spectra for all the catalysts indicated that most of the platinum nanoparticles have an oxidation state of 0. The low-temperature N$_2$ sorption, time-of-flight mass spectrometry, scanning electron microscopy, and transmission electron microscopy experiments have been carried out to characterize the structure of prepared materials. The cyclic voltammetry and rotating disk electrode techniques were used to study the oxygen electroreduction kinetics.

Keywords Platinum nanoparticle size · Oxygen reduction reaction · Carbide-derived carbon · Alkaline fuel cell · Transmission electron microscopy

Introduction

Optimization and design of new catalysts with minimum loading of Pt metal particles have been under discussion for more than two decades. It is well known that size and distribution of the catalyst metal particles on a carbon support, the oxidation state of metal, and the metal support interactions are all important parameters affecting the activity of the oxygen electroreduction process [1–4]. Perez et al. [3] and Geniès et al. [5] have studied particle size effect by comparing different platinum particles supported on various carbon materials and demonstrated that with increase of the Pt particles, the catalyst mass activity decreases. The results established by Cho et al. [6] suggest that the surface area decreases with increasing the platinum loading, and the size of the platinum nanoparticles has been found to change from 3.4 to 5.4 nm if the catalyst loading increases from 20 to 60 wt%, respectively. The importance of the formation conditions and variation of the dispersion step of the Pt nanoparticles deposited onto Vulcan carbon support has been demonstrated by Prabhuram et al. [7]. Higuchi et al. [5] have concluded that if the Pt dispersion state is optimized, then the area-specific oxygen reduction reaction (ORR) activity for Pt–carbon black is independent of the platinum loading within a very wide range (from ~19 to ~63 wt%). On the other hand, the remarkable dependence of the dispersion step of platinum nanoparticles in the catalyst layer is highly affected by the geometrical roughness and porosity characteristics of the support, i.e., by the morphology of the carbon powder used [2]. Nevertheless, the findings reported by Gara et al. [8] contribute to the intense studies of the effect of low or high coverage of platinum loadings on the fuel cell catalyst properties and conclude that the higher particle coverages provide a greater chance of an overall four-electron electroreduction mechanism. Ward et al. [9] and Masa et al. [10] investigated Pt nanoparticle-modified electrodes to evaluate an apparent increase in electrode kinetics due to the surface geometry effects, and they made a detailed analysis of Koutecky–Levich plots; however, this effect has been demonstrated by the authors on flat substrates [8–10]. Therefore, such kind of information is needed for the

E. Härk, R. Jäger, and E. Lust are ISE and ECS members.

E. Härk · R. Jäger · E. Lust (✉)
Institute of Chemistry, University of Tartu, 14a Ravila Str., 50411 Tartu, Estonia
e-mail: enn.lust@ut.ee

porous carbon supports and now analyzed and presented in this paper.

Previous studies [5, 11–22] have demonstrated that ORR can proceed by two pathways in alkaline media. It has been shown by various authors that the contributions of each pathway may vary depending on the reaction conditions applied [3, 11, 15, 23]. However, it is generally accepted that ORR in alkaline media proceeds by a multistep mechanism, involving adsorption and desorption phenomena as a serious complication influencing the activity of the catalysts [3, 24, 25].

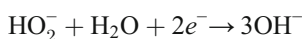The following mechanisms have been proposed for Pt-catalyzed ORR.

Direct four-electron pathway

$$O_2 + 2H_2O + 4e^- \rightarrow 4OH^-$$
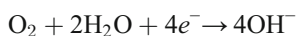
or two-electron pathway with HO_2^- as an intermediate or final product:

$$O_2 + H_2O + 2e^- \rightarrow OH_2^- + OH^-$$
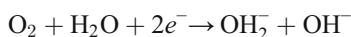
HO_2^- is reduced in an electrochemical reaction as

$$HO_2^- + H_2O + 2e^- \rightarrow 3OH^-$$

or HO_2^- is decomposed

$$HO_2^- \rightarrow OH^- + \frac{1}{2}O_2$$

and the whole ORR process involves also four electrons per oxygen molecule. However, in a porous electrode, H_2O_2 molecule has a high probability to be reduced or decomposed before it desorbs into the solution [5, 8, 13, 15, 26, 27]. It has been emphasized by Genies et al. [13] that, on the smallest Pt nanoparticles, the production of H_2O_2 is very low and the main pathway is the four-electron process. In addition, they stated that probably the amount of H_2O_2 has been produced mainly on the Vulcan-based carbon sites [13]. According to the findings reported by Jaouen et al., the amount of H_2O_2 produced on the carbon site could be electroreduced very quickly forward on the other sites of carbon and, as a result, the produced H_2O_2 does not reach into the electrolyte solution [27].

In our previous papers, we investigated the effect of carbon support on the ORR reaction in acidic [28–30] and alkaline [16, 17, 31] media. In this paper, the influence of Pt loading and particle sizes onto the catalytic activity of ORR has been studied using carbide-derived carbon (C(Mo$_2$C)) and Vulcan XC72® as the catalyst supports. The main difference between

carbide-derived carbon (CDC) and other works is that the average particle size will remain the same with increasing of the Pt loading from 20 to 60 wt% on the CDC support. In addition, it has been demonstrated that at fixed Pt loading, the average size of the Pt nanoparticles can be varied noticeably. However, the gain in decreasing of the metal particle size is not limitless and there is an optimum catalyst particle size for each different type of reaction.

An illustrative scheme, given in Fig. 1, demonstrates some possible situations on the complex catalyst surface. Position 1 describes the ideal case, where uniformly distributed nanoparticles with an average particle size ~5 nm are deposited onto a carbon support, i.e., on the border of the graphitic (conductive part) and amorphous (less conductive) catalyst areas. Thus, if these units are placed side by side each other, the well-defined catalyst monolayer should be formed. However, positions 2A–D illustrate the real cases for the systems developed. Position 2A shows the situation where the nanoparticles with similar average particle sizes are homogeneously distributed onto the carbon support in the case of low Pt nanoparticle loadings (20 wt%) on a carbon surface. Situation B demonstrates the overlapping of nanoparticles and is somewhat similar to the situation described on image C (higher loadings >20 wt%). Situation D describes more likely the bi- or multi-layered Pt catalyst deposited onto the substrate, being valid for rough and porous catalysts (under higher catalyst loading conditions).

One way to achieve a good dispersion of Pt nanoparticles is by using a high surface area carbon support to enhance the dispersion of metal nanoparticles and thereby to increase the effective utilization of the precious metal catalyst [32–34]. However, we should like to emphasize that not only the high
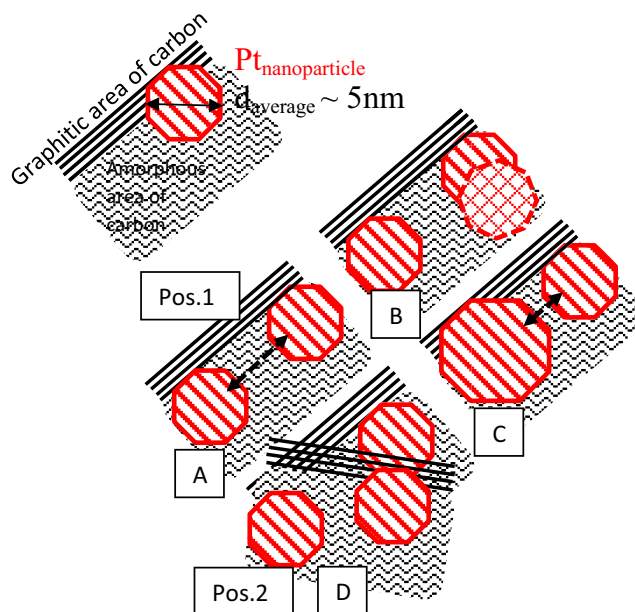

Fig. 1 Illustrative scheme for variable situations for various electroactive surface areas

surface area of a carbon support is important, but also the optimal combination of the pore size distribution, the differential pore volume, and the ratio between graphitized and amorphous carbon areas play the key role in the design of corrosion-resistive as well as electroactive catalysts.

In this work, the porous carbon supports, activated with Pt nanoclusters (20 and 60 wt%), were used as electrodes to study the ORR kinetics using cyclic voltammetry and rotating disk electrode techniques. For comparison, the primary findings have been compared with the results for commercially available Vulcan-based catalysts.

Experimental

Synthesis of Materials

Synthesis of the carbon powder from molybdenum carbide (denoted hereafter as $C(Mo_2C)$) has been fully described previously [16, 17, 28–31, 35]. In short, microporous–mesoporous (MMP) carbon powder was synthesized at a fixed temperature (750 °C) using the high-temperature chlorination technique and then very well cleaned with hydrogen (800 °C, 4 h) and argon [16, 17, 28–31, 35].

The Pt nanoparticles were deposited onto the carbon supports by the sodium borohydride reduction method [24, 36]. The total Pt loading in catalysts synthesized was either ~20 or 60 wt% of the mass of Pt–$C(Mo_2C)$ (named as 20 % Pt–$C(Mo_2C)$ or 60 % Pt–$C(Mo_2C)$-I, respectively). To design the lager nanoparticles on the carbon support, the 60 % Pt–$C(Mo_2C)$-II catalyst was synthesized by a slightly modified procedure—a $NaBH_4$ solution was added to the mixture at a time. The preparation of catalysts under discussion has been previously fully described in [16, 17, 28–31].

The 20 wt% Pt–Vulcan XC72® carbon powder (Fuel Cell Earth, LLC, Wakefield, MA, USA) was used as reference material, named as 20 % Pt–Vulcan. 60 wt% Pt–Vulcan XC72® has been synthesized by using Vulcan XC72® carbon powder (Fuel Cell Earth, LLC, Wakefield, MA, USA) and named as 60 % Pt–Vulcan.

Preparation of the Electrodes

Cyclic voltammetry (CV) and the rotating disk electrode (RDE) methods have been used for the electrochemical analysis. The catalyst sample was deposited onto a glassy carbon disk electrode (GCDE) (Pine Instrument Company) with a geometric surface area of 0.196 cm², pressed into a Teflon holder [16, 17, 28–31]. The catalyst ink was prepared by mixing carbon powder modified with Pt nanoclusters with the Nafion® dispersion solution (5 wt%, Aldrich), to give a dry catalyst with a fixed (5 %) composition of Nafion® ionomer, and sonicated for 1 h at room temperature to obtain a uniformly dispersed ink. Thereafter, 9 μl of ink was deposited onto the GCDE surface to form a catalyst layer and left to dry at room temperature. The loading of the catalyst was approximately 1.00±0.02 mg cm⁻² (the estimation of reproducibility is based on a series of five independent experiments).

Electrochemical and Physical Characterization of Catalysts

Electrochemical analysis was carried out in a three-electrode electrochemical cell [16, 17, 28–31, 37–41] using a rotating disk electrode system (Gamry Instruments Inc., Reference 600™). The counter electrode was a very large Pt wire mesh ($S_{Pt} \geq 50$ cm²). All potentials were measured against a Hg|HgO| 0.1 M KOH reference electrode (denoted as Hg|HgO (0.171 V vs. SHE)) connected to the cell through a long Luggin capillary. The 0.1 M KOH solution was prepared from solid KOH (Sigma-Aldrich, 99.99 %) and ultrapure Milli-Q⁺ water.

The catalyst-coated GCDE was submerged under a standby potential into 0.1 M KOH electrolyte solution previously saturated for 30 min with Ar (99.9999 %, The Linde Group, AGA). The selected standby potential was 0.21 V (vs. Hg|HgO), where the current densities for ORR, measured by the RDE method, were minimal. In order to achieve a stable surface state, the working electrodes were cycled prior to measurements in Ar-saturated aqueous alkaline solution for at least 30 min, and more than seven potential cycles have been made within the potential (E) region from 0.31 to −0.55 V (vs. Hg|HgO). Thereafter, the CVs were measured at different potential scan rates, v, from 5 to 200 mV s⁻¹ (the so-called background current densities). After CVs, the RDE voltammetry curves (at rotation velocities from 0 to 3000 rev min⁻¹) were measured at v=10 mV s⁻¹.

As a next step, the solution was saturated with molecular O_2 (99.999 %, The Linde Group, AGA) for 30 min, and the RDE data at 10 mV s⁻¹ and CVs at a different v from 5 to 200 mV s⁻¹ were collected. For equilibration of the electrode properties, the RDE was cycled at least five times within the region of E from 0.31 to −0.55 V (vs. Hg|HgO) at a constant rotation velocity of 800 rev min⁻¹ before RDE measurements at different rotation velocities. Thereafter, the RDE measurements were conducted at different RDE rotation velocities to study the ORR kinetics [41–43].

All measurements were carried out at temperature 22± 1 °C, and at least five different electrodes, prepared at identical conditions, were used.

Synthesized catalysts were physically characterized by using, the low-temperature N_2 sorption, scanning electron microscopy (SEM), and transmission electron microscopy (TEM) methods [16, 17, 28–31, 35].

The X-ray diffraction (XRD) patterns for the catalysts were collected applying a Bruker D8 Advance diffractometer with

Ni-filtered CuK_α radiation [17]. The characterization of the catalyst powder surfaces has been determined by a time-of-flight secondary ion mass spectrometer (TOF-SIMS; PHI TRIFT V nanoTOF) and using Ga$^+$ 30-keV primary ions. The X-ray photoelectron spectroscopy (XPS) experiments were carried out with a SCIENTA SES-100 spectrometer. For the detailed TOF-SIMS and XPS measurements, the catalyst powders were pressed onto an indium surface.

Results

X-ray Diffraction Analysis

The XRD patterns for the carbon-supported catalyst materials are shown in Fig. 2. The data have been treated using the Debye–Scherrer equation [36], and the calculated average particle sizes of the Pt nanoparticles are given in Table 1. Diffractograms in Fig. 2 show that intensities of the Pt peaks increase with the Pt average nanoparticle size in the catalysts. It should be noted that the peak width decreases, especially for the Pt[111] orientation, and becomes sharper with increasing of the Pt nanoparticle (Fig. 2).

A comparison of the XRD patterns for the carbon-supported catalysts (Fig. 2 inset) shows that the intensities of the Pt peaks increase with the Pt loading in materials, but the calculated average particle size d, given in Table 1, only slightly depends on the weight percent of the Pt nanoparticles deposited. Very high surface areas (S_A) for Pt nanoparticles (67 m^2 g^{-1} for 20 % Pt–C(Mo$_2$C) and 58 m^2 g^{-1} for 60 % Pt–C(Mo$_2$C)-I (Table 1)) have been calculated by the method described by Álvarez et al. [36]. For Vulcan-based electrodes, the S_A values calculated are somewhat lower.

An extremely low surface area ($S_A=10$ m^2 g^{-1}) has been established for 60 % Pt–C(Mo$_2$C)-II with the average particle size of 27.2 nm (Table 1). Thus, the surface area of Pt nanoparticles is higher for the catalysts with lower d values, in a good agreement with the results of Cho et al. [6].

X-ray Photoelectron Spectroscopy Analysis

The XPS data for C(Mo$_2$C) and 20 % Pt–C(Mo$_2$C) catalysts are given in Fig. 3. The following scanning parameters have been used: energy range from 600 to 0 eV, pass energy= 200 eV, step size=0.5 eV (Fig. 3a, b). Wide-range scans by XPS of the C(Mo$_2$C) catalyst material surfaces show the presence of carbon (C1s), oxygen (O1s), indium (In3d) (Fig. 3a), and C1s, O1s, In3d, platinum (Pt4d, Pt4f) for 20 % Pt–C(Mo$_2$C) (Fig. 3b). The XPS survey scans show a quite simple oxygen (O1s) peak at 532 eV, which is probably related to the adsorbed oxygen (Fig. 3a, b) [44, 45]. For the high-resolution scans, the following parameters were used: energy range from 295 to 275 eV for C1s and from 82 to −65 eV for Pt4f regions, respectively, pass energy=200 eV, step size=0.1 eV (Fig. 3c, d). Based on the XPS data analysis (shown in Fig. 2d), two different Pt4f peaks with the binding energies 71.2 eV (4f$_{7/2}$) and 74.4 eV (4f$_{5/2}$), respectively, are well resolved being in a good agreement with literature data [4, 44, 45]. The results reported by other authors reveal that the lower binding energy is due to an extensive Pt(0) state, while the higher binding energy component is due to the Pt(IV) species (PtO$_2$ or Pt(OH)$_4$, presented at the catalyst surface) [2, 4]. However, it is difficult to identify exactly which oxygen-containing groups are bonded to the platinum surface. It has been also shown that the majority of the oxygen-containing groups were affected by the attached oxygen to the carbon support [4, 44, 45].

Fig. 2 X-ray diffraction data for various Pt-modified systems: *1* 60 wt% Pt–Vulcan; *2* 60 wt% Pt–C(Mo$_2$C)-I; *3* 60 wt% Pt–C(Mo$_2$C)-II. *Inset*: *1* 60 wt% Pt–C(Mo$_2$C)-I; *2* 20 wt% Pt–C(Mo$_2$C); *3* 60 wt% Pt–Vulcan; *4* 20 wt% Pt–Vulcan
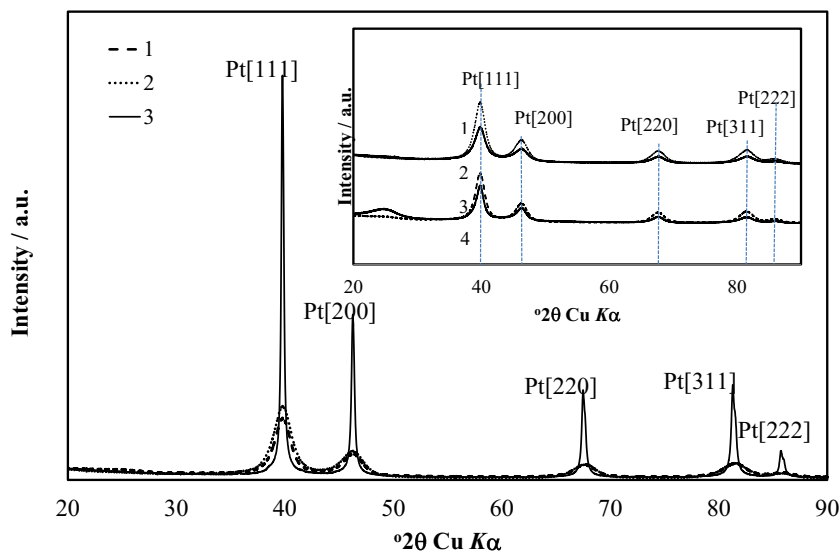
Table 1 Physicochemical properties of catalysts

Catalyst	a (Å)	d (Å)	S_A (m² g⁻¹)	A_{eff} (cm²)
20 % Pt–C(Mo₂C)	3.912±0.032	42.4±0.5	66.0±0.8	0.617±0.1
60 % Pt–C(Mo₂C)-I	3.914±0.016	47.8±0.2	58.5±0.5	0.272±0.05
60 % Pt–C(Mo₂C)-II	3.920±0.018	272.2±0.2	10.28±0.01	0.309±0.05
20 % Pt–Vulcan	3.911±0.029	57.7±0.5	48.5±0.5	0.407±0.08
60 % Pt–Vulcan	3.915±0.016	54.0±0.2	51.8±0.2	0.272±0.05

a lattice parameter, *d* average crystallite size, S_A surface area of metallic nanoparticles, A_{eff} effective electrochemical surface area
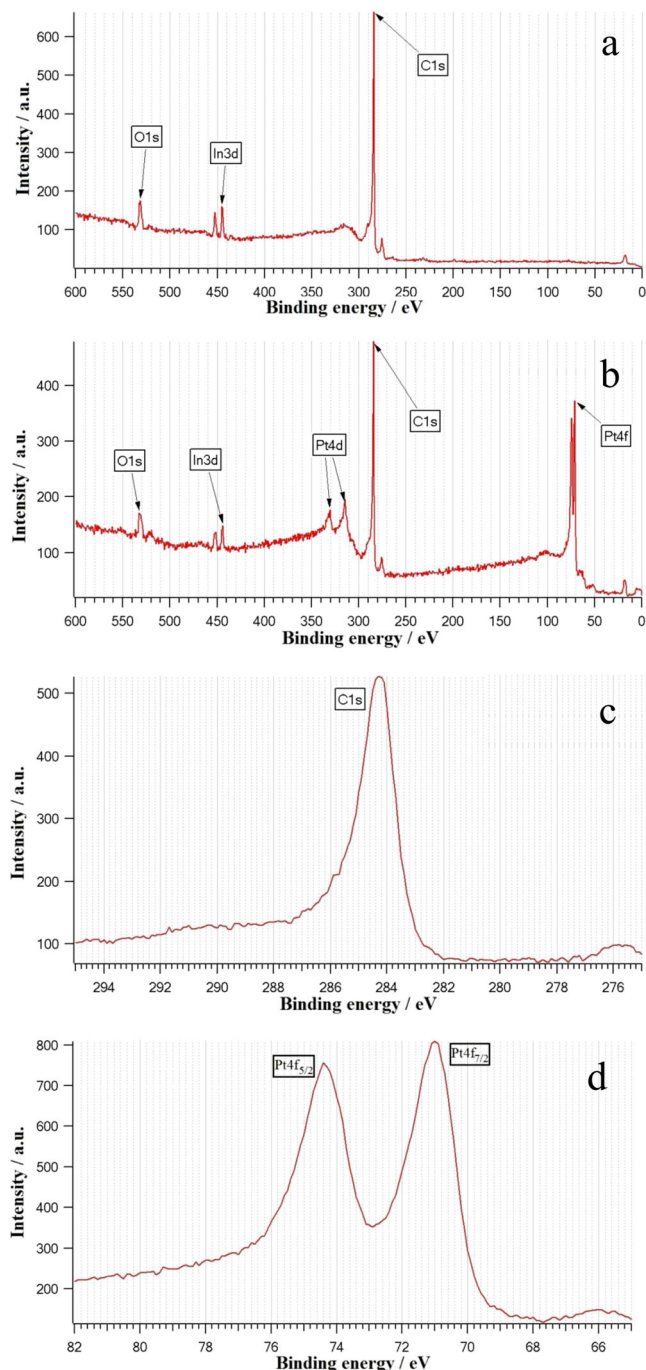

Fig. 3 XPS spectra of catalyst **a** C(Mo₂C) and **b** 20 wt% Pt–C(Mo₂C). Detailed XPS spectra of C1s **c** and Pt4f **d** regions for the 20 wt% Pt–C(Mo₂C) catalyst

Time-of-Flight Mass Spectrometry Analysis

Based on our previous papers, the carbon support derived from molybdenum carbide has a noticeably higher catalytic activity towards ORR than the Vulcan sample [17, 31]. It has been suspected that this effect could be due to the presence of traces of some Mo or other impurities on the carbon support surface (like Cl₂). Therefore, the surface chemical composition of the C(Mo₂C) has been specially studied using the time-of-flight mass spectrometry method (Fig. 4). The surface images of various catalysts are given in Fig. 4a. Negative and positive secondary ions in the mass range from 0 to 400 amu/z were analyzed in areas of 25×25 μm² using a raster of 512×512 measured points. The partial positive TOF-SIMS spectra indicate that $^{70}Cl_2$, ^{98}Mo, $^{208}Mo_2C$, and $^{273}MoCl_5$ have not been observed within the 50–400-amu range measured. Detailed compositional isotope analysis of the catalyst samples within the 180–200-amu range indicates that 60 % Pt–Vulcan has the same variety of Pt isotopes (i.e., typically 194, 195, 196, 198) as the Pt–C(Mo₂C)-I and Pt–C(Mo₂C)-II catalysts.

Low-Temperature N₂ Sorption Analysis

The specific surface area (S_{BET}) has been calculated according to the Brunauer–Emmett–Teller (BET) multipoint theory within the relative pressure range from 0.05 to 0.2, and the values established are given in Table 2. The total volume of pores (V_{tot}) has been calculated at a relative pressure (0.95), and the micropore volume (V_{micro}) has been obtained using the t-plot method completed with the Harkins and Jura thickness values for the adsorption layer thickness between 5 and 90 Å. The non-local density functional theory completed with the slit shape pore model, applicable for MMP materials [32, 46, 47], has been used for the pore width calculations. The results of sorption measurements show that the BET surface area for C(Mo₂C) powder is 2020 m² g⁻¹ and the pore size distribution maxima locate within 0.8–1.2 and 2–8-nm regions, respectively, indicating that C(Mo₂C) is a microporous–mesoporous electrode material. Figure 5 illustrates that the Vulcan-based powders have the pore size distribution maxima within 0.8–1.2 and 10–50-nm regions, respectively.

The noticeable decrease of S_{BET}, S_{micro}, V_{micro}, and V_{tot} takes place as a result of the Pt nanocluster deposition onto/
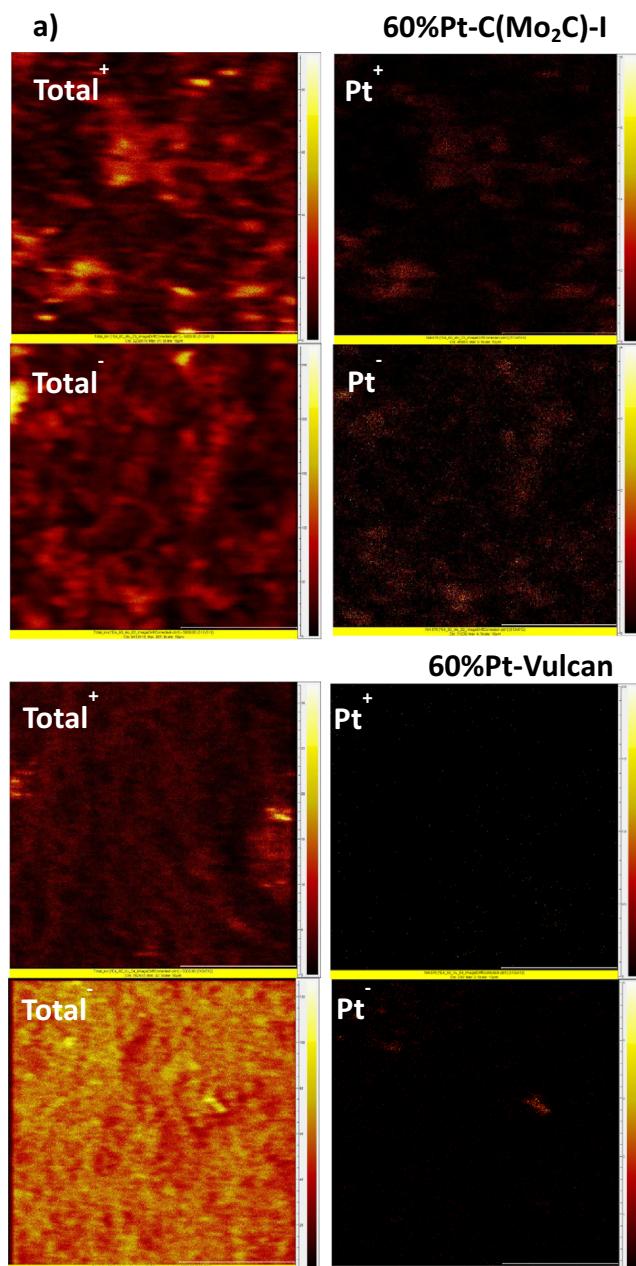
Fig. 4 TOF-SIMS images (field of view 25 μm) for various Pt-modified systems **a**; TOF-SIMS spectra of the catalyst (noted in figure) partial positive within the mass range 50–100 **b** and partial negative within the mass range 180–200 **c**

of the average particle size or carbon support used. Due to the differences between mesoporous areas in $C(Mo_2C)$ and Vulcan-based catalysts (2–8 and 10–50-nm regions, respectively), we can also observe the slight differences in electrochemical activities and the calculated values of the effective electrochemically active surface areas, described in details later (Table 2).

Scanning Electron Microscopy Analysis

Figure 6 illustrates the SEM images for studied materials, demonstrating that the structural integrity is still very well reserved even after the increase of the catalyst loading up to 60 wt%. Small Pt nanoparticles are uniformly dispersed onto/ into the carbon particles, which imply that the change of the metal loading does not have a significant effect on the distribution of the Pt nanoparticles. The particle sizes measured directly from SEM images (20 % Pt–$C(Mo_2C)$, 60 % Pt–$C(Mo_2C)$-I, and 60 % Pt–Vulcan) at randomly selected regions were approximately ~5 nm, confirming the values determined from the XRD results (Table 1).

Transmission Electron Microscopy Analysis

The morphology of the supported catalysts were observed by transmission electron microscopy (TEM) using a FEI Tecnai T12 apparatus [17, 28–30]. TEM analysis of the catalysts (Fig. 7) shows a Pt nanoparticle size distribution similar to that found by XRD and SEM measurements (Table 1) and a homogeneous distribution of fine Pt metal nanoparticles on the various carbon supports. Histograms of the particle size distribution for catalysts have been established within a narrow size range from 3 to 5 nm (average particle size 4.50± 0.05 nm) [17]. The high-resolution TEM, XPS, and TOF-SIMS data confirm the absence of Mo, Mo_2C, $MoCl_5$, and Cl_2 at/inside the porous carbon powders in good agreement with X-ray fluorescence and Raman spectroscopy data (not discussed and shown here).

RDE Analysis of O_2 Reduction Reaction

The experimental current densities vs. electrode potential (j, E) measurements were carried out without the ohmic potential drop (iR) compensation [19]. However, according to our previous works [16, 17], it is important to take into account the iR drop values. Therefore, in this paper, all data presented are corrected against the ohmic potential drop. The RDE data were additionally corrected for the background current densities measured in the respective Ar-saturated KOH electrolyte solution.

The polarization curves in 0.1 M KOH solution (current density (j_c) vs. electrode potential (E)) recorded for materials with various Pt loadings (20 and 60 wt%) are given in Fig. 8.

into $C(Mo_2C)$ supports (Table 2). As expected, the surface areas and pore volumes for Pt nanocluster-modified $C(Mo_2C)$ powders were noticeably higher compared with those for the Pt nanocluster-modified Vulcan electrodes, respectively. It should be noted that based on the analysis of the sorption data (Table 2), the surface area and total pore volume values decrease remarkably, if the Pt loading increases from 20 to 60 %. An especially noticeable decrease of the micropore volume has been established with the increase of the Pt nanoparticle loading from 20 to 60 wt% despite the constancy
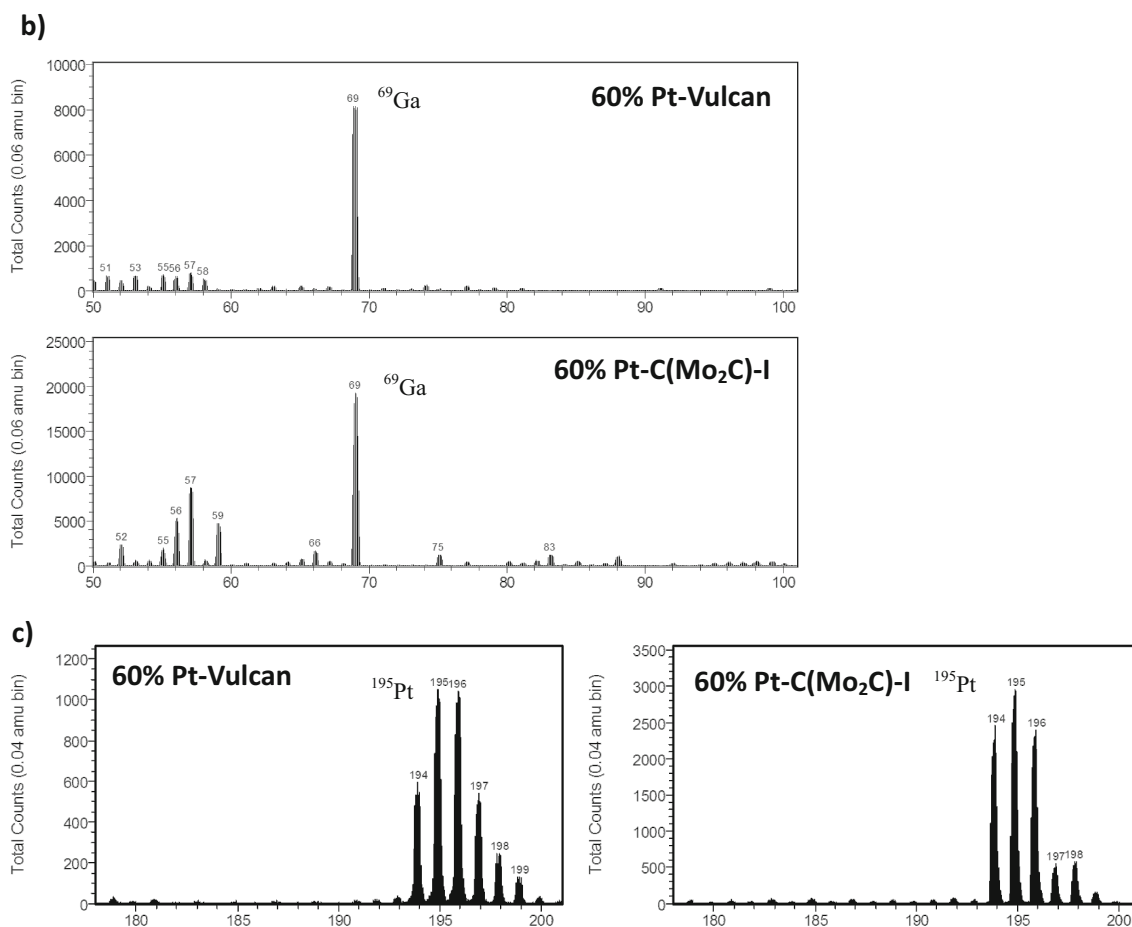
b)

c)

Fig. 4 (continued)

At negative electrode potentials ($E \leq -0.30$ V (vs. Hg|HgO)), the current densities are mainly limited by the mass transport (O$_2$ diffusion) process from the solution to the electrode surface [16–20]. According to the RDE theory, the limiting current density $|j_{lim}|$ value has been calculated, applying Eq. (1)

$$j_{lim} = 0.62nFD^{2/3}v^{-1/6}C\omega^{1/2} \qquad (1)$$

Table 2 Results of sorption measurements

Sample	S_{BET} (m^2 g^{-1})	S_{micro} (m^2 g^{-1})	V_{micro} (cm^3 g^{-1})	V_{tot} (cm^3 g^{-1})
C(Mo$_2$C)	2020	1660	1.07	1.83
20 % Pt–C(Mo$_2$C)	1600	1367	0.89	1.37
60 % Pt–C(Mo$_2$C)-I	800	560	0.33	0.80
60 % Pt–C(Mo$_2$C)-II	590	480	0.31	0.54
Vulcan	240	144	0.07	0.52
20 % Pt–Vulcan	180	107	0.05	0.41
60 % Pt–Vulcan	110	50	0.02	0.44

S_{BET} BET surface area, S_{micro} micropore area calculated using the t-plot method, V_{micro} micropore volume, V_{tot} total pore volume

using the number of electrons transferred per oxygen molecule reduced ($n=4$), the diffusion coefficient ($D=1.8 \cdot 10^{-5}$ cm^2 s^{-1}), the kinematic viscosity of the solution ($v=0.01$ cm^2 s^{-1}), and the oxygen concentration ($C=1.13$ mM) [10, 36]; F is the Faraday constant and ω is the rotation velocity of the electrode (rad s^{-1}). The calculated

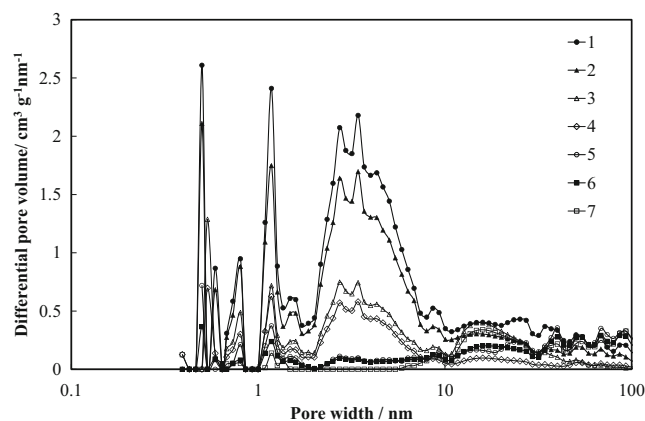**Fig. 5** Differential pore volume vs. pore width plots analyzed with low-temperature nitrogen adsorption/desorption method for catalysts: *1* C(Mo$_2$C); *2* 20 wt% Pt–C(Mo$_2$C); *3* 60 wt% Pt–C(Mo$_2$C)-I; *4* 60 wt% Pt–C(Mo$_2$C)-II; *5* Vulcan; *6* 20 wt% Pt–Vulcan; *7* 60 wt% Pt–Vulcan

Fig. 6 SEM images for **a** 20 wt% Pt–C(Mo$_2$C); **b** 60 wt% Pt–C(Mo$_2$C)-I; **c** 60 wt% Pt–C(Mo$_2$C)-II; and **d** 60 wt% Pt–Vulcan
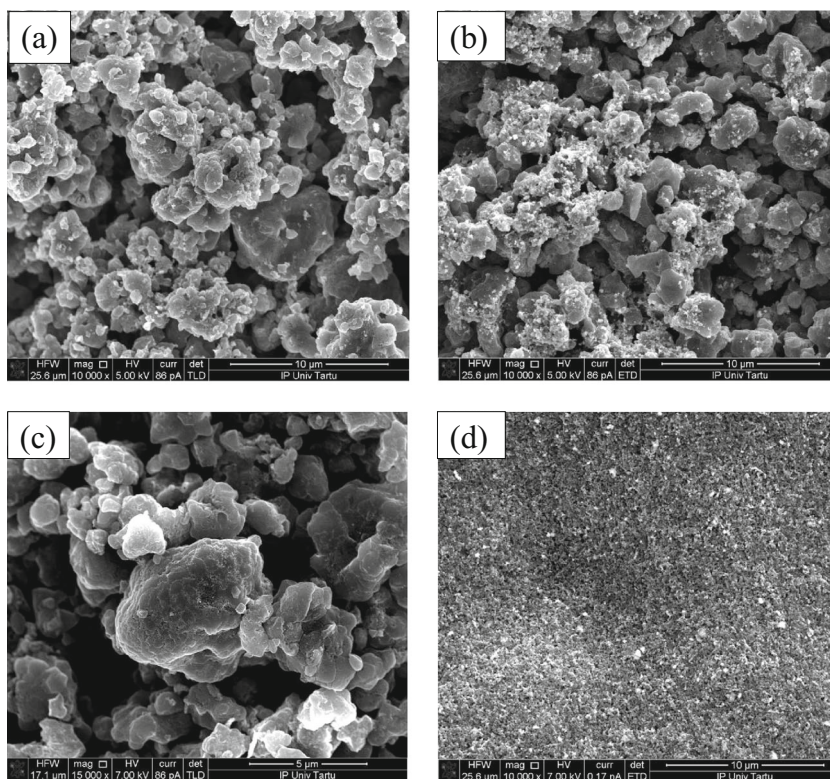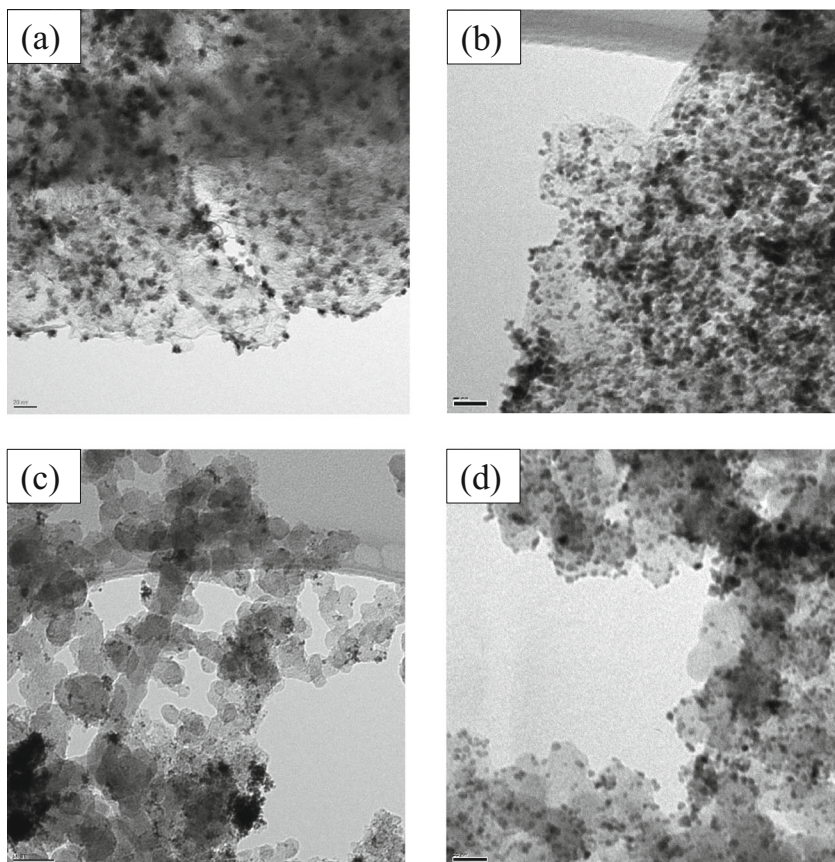

Fig. 7 TEM images for **a** 20 wt% Pt–C(Mo$_2$C); **b** 60 wt% Pt–C(Mo$_2$C)-I; **c** 20 wt% Pt–Vulcan; and **d** 60 wt% Pt–Vulcan
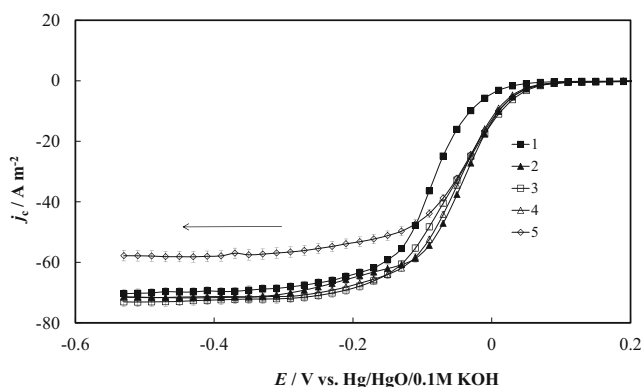
Fig. 8 RDE data for ORR (corrected for current densities in base electrolyte solution saturated with Ar) in 0.1 M KOH saturated with O_2 at electrodes: *1* 20 wt% Pt–Vulcan; *2* 20 wt% Pt–C(Mo_2C); *3* 60 wt% Pt–Vulcan; *4* 60 wt% Pt–C(Mo_2C)-I; and *5* 60 wt% Pt–C(Mo_2C)-II (potential scan rate ν=10 mV sec^{-1}, rotation speed 3000 rev min^{-1})

$|j_{lim}|$=70.92 A m^{-2} is in a good agreement with current densities $|j_c|$ at an electrode potential $E \leq -0.30$ V (vs. Hg|HgO). It was established that within the region of diffusion limitation (from −0.30 to −0.55 V (vs. Hg|HgO)), the differences between the limiting current density values for the Pt nanoparticle-activated carbons with the similar average particle size were minimal (Fig. 8). However, the limiting current densities decrease with increasing the average Pt nanoparticle size (Fig. 8, line 5). This could be caused by the lower surface area of the metallic Pt nanoparticles (S_A) in a catalyst, calculated from XRD data (Table 1). In addition, in the case of the catalyst with lager Pt nanoparticles (Pt–C(Mo_2C)-II), the diffusion-limited current value is probably influenced by the carbon surface area free of Pt nanoparticles.

The number of electrons (n=4) transferred per oxygen molecule has been calculated, being in an agreement with the data for other Pt nanoparticle-modified microporous–mesoporous carbon electrodes, indicating that the four-electron transfer mechanism is mainly valid for Pt nanocluster-activated carbons with the smaller Pt nanoparticles available on the surface [5, 12].

Various authors investigating the geometrically rough and porous (non-flat) and energetically (in addition to geometric inhomogeneity) non-uniform electrodes have proposed several hypotheses, simulations, and solutions on how to take into account the real, i.e., effective, electroactive surface area of the catalyst [8–10]. Masa et al. [10] proposed a way how to estimate the electrocatalytic activity based on the Koutecky–Levich analysis of the RDE data. They analyzed the influence of the ratio between the surface area of the electroactive nanoparticles and the geometric area of the substrate glassy carbon electrode. They concluded that this ratio does not affect the diffusion-limited currents, i.e., the hydrodynamic requirements remain valid and the Koutecky–Levich method can be used for determination of the n values [10]. However, for reactions controlled by mixed kinetics, thus, by diffusion

and charge transfer steps, a more detailed analysis should be considered. Therefore, in this paper, we have proposed also an approach to estimate the effective surface area (A_{eff}) through the Randles–Sevcik analysis. This new approach showed very interesting results and is discussed in more details later.

The mixed mass transport/kinetically controlled region was established within the potential region from −0.30 to 0.05 V (vs. Hg|HgO). The kinetic current densities (j_{kin}) were calculated from the intercept j_c^{-1} vs. $\omega^{-1/2}$ dependences and used for further analysis. The Pt metal loading plays a remarkable role in the case of the Vulcan-based electrodes within the mixed kinetic region of ORR (Fig. 8). In contrast, for the Pt–C(Mo_2C) electrodes activated with 20 or 60 wt% Pt nanoclusters, there are minor changes in catalytic activity, indicating that the 60 % Pt–C(Mo_2C)-I and 60 % Pt–C(Mo_2C)-II are overloaded with Pt nanoclusters (Fig. 8). Within the mixed kinetic region, the catalytic activity towards ORR is independent of the average Pt nanoparticle size in catalysts. It is obvious from Fig. 8 that the carbon support does not play a significant role in the case of higher Pt loadings.

The calculated Tafel-like plots for the electrodes studied are presented in Fig. 9. The ORR overvoltage is higher (catalytic activity is lower) for the 20 % Pt–Vulcan electrode compared with other systems. The slope value of the Tafel-like plot (81±3 mV dec^{-1}) has been obtained for the 20 % Pt–Vulcan electrode, but for other catalysts, the slope values calculated are higher, being −90±3 mV dec^{-1} [48]. This is probably due to the fact that the electrocatalytic activity depends on the coverage of oxygen on the platinum surface [3, 12] and there are small Pt nanoparticle size changes depending of the catalyst support used (Table 1), causing a weak influence on the mass transfer and charge transfer kinetics overall, especially at lower Pt loadings for Vulcan-based catalysts.
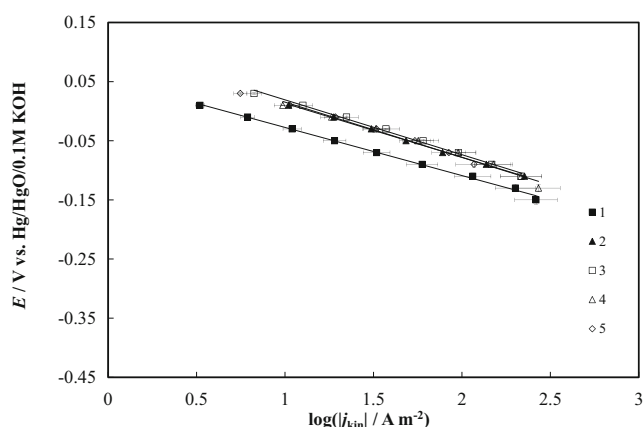

Fig. 9 Tafel-like plots calculated from RDE data in 0.1 M KOH solution saturated with O_2 for electrodes: *1* 20 wt% Pt–Vulcan; *2* 20 wt% Pt–C(Mo_2C); *3* 60 wt% Pt–Vulcan; *4* 60 wt% Pt–C(Mo_2C)-I; *5* 60 wt% Pt–C(Mo_2C)-II

According to the findings presented in a previous work [17], we can conclude that the role of the carbon support decreases if the Pt loading in the catalyst material increases. In the present paper, the current density values for 60 % Pt–C(Mo$_2$C)-I and 60 % Pt–Vulcan with similar Pt nanoparticle sizes coincide (Fig. 8). Therefore, the amount of the deposited platinum is too high and, in the mixed kinetic region, the charge transfer and the mass transport processes are determined solely by the platinum nanoparticles.

The effect of Pt loading has been analyzed by constructing the corrected Tafel-like plots using the calculated effective electrochemically active surface area values (discussed in more detail later), which differ from the geometric area of the rotating disk surface (Fig. 10a). Figure 10b shows the recalculated kinetic current density values using the surface area of metallic nanoparticles (S_A) obtained from XRD data and given in Table 1. This approach takes into account only the Pt nanoparticle size effect towards ORR. It is obvious that catalysts with the smaller average particle sizes have higher catalytic activity towards ORR.
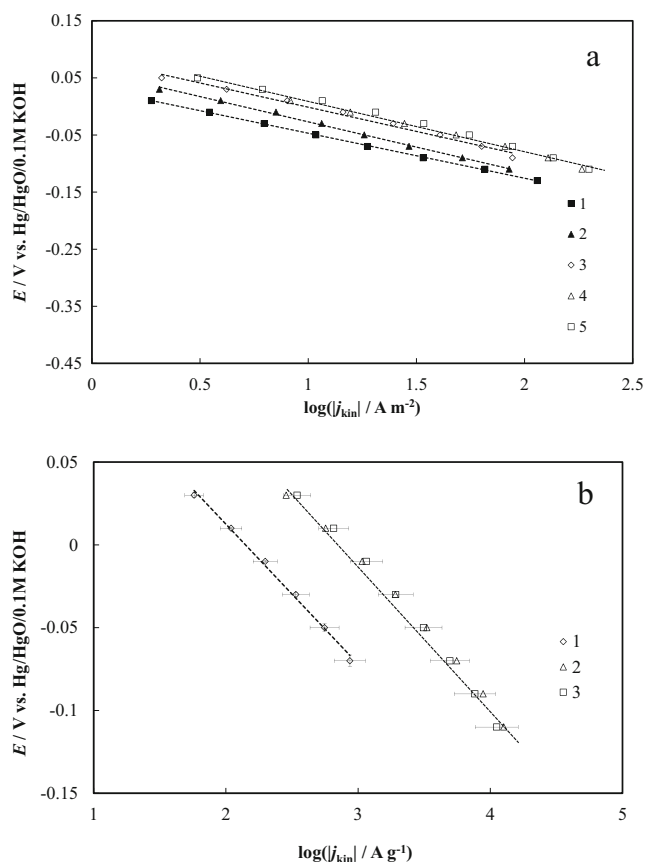
Cyclic Voltammetry Measurements

The cyclic voltammograms were recorded at fixed potential scan rates (ν=5, 10, 20, 30, 50, 70, 100, 150, and 200 mV s^{-1}) in both Ar- and O$_2$-saturated solutions. The CV curves measured and calculated into the capacitance scale for various catalysts studied showed a different capacitive behavior (Fig. 11). The capacitance of the catalyst material (C_{cv}) increases in the following sequence: 60 % Pt–Vulcan, 20 % Pt–Vulcan, 60 % Pt–C(Mo$_2$C)-II, 60 % Pt–C(Mo$_2$C)-I, and 20 % Pt–C(Mo$_2$C). Therefore, the differences in the contribution of various carbon supports (Vulcan and C(Mo$_2$C)) to the pseudocapacitative (i.e., faradaic capacitance) behavior is clearly demonstrated and it is very important for applications like supercapacitors, batteries, and hybrid fuel cells. The reduction peak potentials (E_p) are shifted towards more positive electrode potentials with the increase of the Pt loading in a catalyst. With the decrease of the average Pt nanoparticle size, E_p is shifted towards more positive electrode potentials. However, the influence of the average Pt nanoparticle size on E_p is small. The pseudocapacitative behavior for various catalysts is somewhat affected by the differences in the carbon support porosity, pore size distribution, and S_{BET}. The dependence of the C_{cv} within the electrode potential range (-0.55 V$<E<$ -0.33 V) is in accordance with the values of S_{BET} and S_{micro}. In order to evaluate correctly the contribution of the kinetic currents of the catalysts, the presented cyclic voltammetry data have been corrected against the ohmic potential drop and for the background current densities in the respective Ar-saturated KOH supporting electrolyte solution [16, 17].

The corrected cyclic voltammetry data for the Pt–C(Mo$_2$C)-II catalyst are shown in Fig. 12. There are very well expressed reduction peaks in j_c, E curves for cathodic potential sweep direction. The peak potentials (E_p) and reduction peak current density values (j_{peak}) depend on the potential scan rate
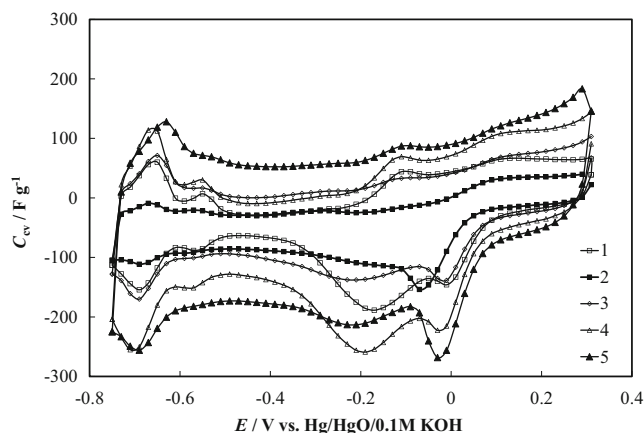

Fig. 10 a Tafel-like plots corrected with the calculated A_{eff} values for electrodes: *1* 20 wt% Pt–Vulcan; *2* 20 wt% Pt–C(Mo$_2$C); *3* 60 wt% Pt–C(Mo$_2$C)-II; *4* 60 wt% Pt–C(Mo$_2$C)-I; *5* 60 wt% Pt–Vulcan. b Tafel-like plots corrected with the S_A values for electrodes: *1* 60 wt% Pt–C(Mo$_2$C)-II; *2* 60 wt% Pt–C(Mo$_2$C)-I; *3* 60 wt% Pt–Vulcan

Fig. 11 Calculated capacitance C_{cv} vs. E plots (at ν=5 mV s^{-1}) for various systems in 0.1 M KOH solution saturated with O$_2$: *1* 60 wt% Pt–Vulcan; *2* 20 wt% Pt–Vulcan; *3* 60 wt% Pt–C(Mo$_2$C)-II; *4* 60 wt% Pt–C(Mo$_2$C)-I; *5* 20 wt% Pt–C(Mo$_2$C)
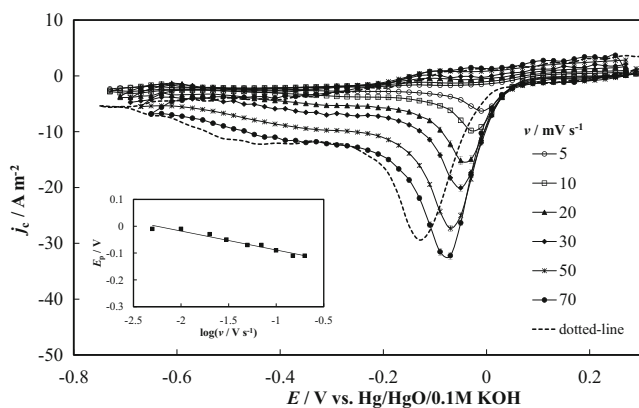
Fig. 12 j_c vs. E plots at various potential scan rates (noted in figure) for the Pt–C(Mo$_2$C)-II electrode in 0.1 M KOH solution saturated with O$_2$ (currents were corrected for current densities in 0.1 M KOH solution, saturated with Ar). CV curve without iR drop compensation (*dotted line*) at a potential scan rate of 70 mV s^{-1}. *Inset*: peak potential vs. logarithm of the scan rate dependence calculated from the CV curves

Fig. 13 j_c vs. E plots for 20 wt% Pt–C(Mo$_2$C) (*1*) and 60 wt% Pt–C(Mo$_2$C)-I (*2*) in 0.1 M KOH solution saturated with O$_2$ at potential scanning rate v=5 mV s^{-1} (currents were corrected for current densities in 0.1 M KOH solution, saturated with Ar). *Inset*: Randles–Sevcik plots (peak current vs. square root of the scan rate) calculated from the CV curves for electrodes: *1* 20 wt% Pt–C(Mo$_2$C); *2* 20 wt% Pt–Vulcan; *3* 60 wt% Pt–C(Mo$_2$C)-I; *4* 60 wt% Pt–Vulcan

(ν). Reduction peak current density values increase and the peak potentials shift towards more negative electrode potentials with increasing ν (Fig. 12). As shown in the inset of Fig. 12, the E_p against logν plot is linear, which confirms that ORR is an irreversible process.

According to the Laviron theory [49] modified by Gara et al. [50], the electron transfer coefficient value was calculated using Eq (2):

$$E_p = E^\circ - \frac{RT}{\propto nF}\left[0.780 - \ln(k) + \ln\left(\sqrt{\frac{\propto nFD\upsilon}{RT}}\right)\right] \quad (2)$$

where k is the apparent electrochemical rate constant of the reaction and E° is the formal electrode potential.

The cyclic voltammograms (ν=5 mV s^{-1}) for the 20 and 60 % Pt–C(Mo$_2$C)-I electrodes (Fig. 13) illustrate that the reduction peak current density values for 20 % Pt–C(Mo$_2$C) are nearly two times higher compared with those for the 60 % Pt–C(Mo$_2$C)-I electrode. For all materials studied, the reduction peak current density values ($|I_{peak}|$) increase nearly linearly with the square root of the scan rate ($\nu^{1/2}$) (inset of Fig. 13). The effective electrochemical surface area values (A_{eff}) were obtained using the Randles–Sevcik equation:

$$I_{peak} = -0.496nFA_{eff}C\sqrt{\frac{\propto nF\upsilon D}{RT}} \quad (3)$$

where I_{peak} is the peak current, n is the number of electrons transferred per oxygen molecule reduced (n=4), $\propto$ is the electron transfer coefficient, F is the Faraday constant, T is the temperature, R is the gas constant, D is the diffusion coefficient ($1.8 \cdot 10^{-5}$ cm^2 s^{-1}), and C is the oxygen
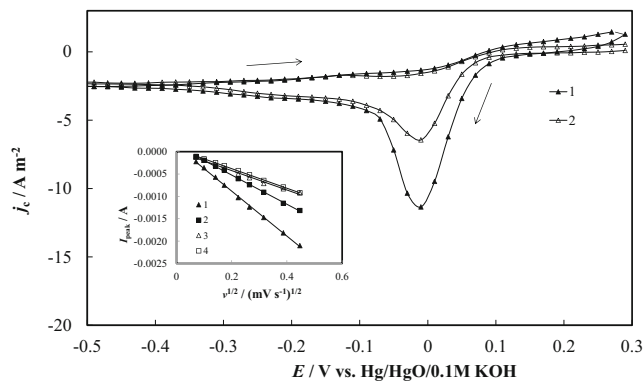
concentration (1.13 mM) [14, 15, 17, 42, 43]. The calculated effective electrochemical surface area values are given in Table 1. The increase of platinum amount from 20 to 60 wt% causes the decrease of the calculated effective electrochemically active surface area (A_{eff}). The calculated values of A_{eff} depend strongly on the carbon support parameters. The location and distribution of the Pt nanoparticles on the carbon support, i.e., distance between the two nanoparticles (Fig. 1 pos. 1 and 2), differ. For both 60 wt% Pt–C(Mo$_2$C)-I and 60 wt% Pt–C(Mo$_2$C)-II catalysts, the calculated A_{eff} is relatively close to the geometric surface area (0.196 cm^2) due to the fact that the catalyst surface is overloaded with deposited platinum nanoparticles, i.e., the catalyst is acting as a flat or nearly smooth electrode. The same effect has been established for the 60 % Pt–Vulcan electrode (Table 1). The importance of the differences between the geometric electrode area and the total active surface area of the catalyst has been described by Masa et al. [10].

The decrease in particle size of the Pt nanoclusters causes an increase in the activity of the catalyst due to an increase in the active surface area (S_A) of the catalyst (Table 1). It is not only the gain in decreasing the metal particle size that is limited; but it is also because there is an optimum mesoporous/microporous area (active sites) available on the carbon support.

Conclusions

The influence of loading of the Pt nanoparticles deposited onto various microporous–mesoporous carbon supports on ORR has been analyzed by comparing the various carbon-supported Pt (20 and 60 wt% metal) catalysts in 0.1 M KOH aqueous solution. The influence of the average Pt nanoparticle

size has been demonstrated. A new approach for estimation of the electrochemically active surface area has been discussed and the results have been demonstrated.

Physical analysis using XRD, XPS, TOF-SIMS, low-temperature N_2 sorption, SEM, and TEM methods of the various carbon-supported Pt nanocluster-activated (20 and 60 wt% metal) materials has been made and can be summarized as follows:

1. XRD, SEM, and TEM results for catalysts reveal that the platinum nanoparticles with a smaller average particle size (45.0±0.5 Å) are homogeneously dispersed onto the different carbon supports used.
2. XPS data indicate that most of the platinum nanoparticles have an oxidation state of 0 and a small amount have a +4 oxidation state with binding energies of 71.2 eV (Pt4f$_{7/2}$) and 74.4 eV (Pt4f$_{5/2}$), respectively.
3. The decrease in platinum amount from 60 to 20 wt% causes the increase in calculated effective electrochemically active surface area values (A_{eff}). For all 60 wt% Pt catalyst, the values of A_{eff} are relatively close to the geometric surface area, i.e., the catalysts are acting as a nearly flat and/or smooth electrode.
4. It was established that the ORR activity for 20 wt% Pt–C(Mo$_2$C) is comparable with 60 wt% Pt–Vulcan catalytic activity. Therefore, a smaller Pt loading is required for effective ORR at microporous–mesoporous carbide-derived carbon (C(Mo$_2$C))-supported electrodes, compared with Vulcan-based catalysts.
5. The corrected Tafel-like plots coincide for the catalysts with 60 % Pt loading if the A_{eff} values were used for correction of the experimental data. Taking into account the effective electrochemically active surface area instead of the geometric electrode surface area, the catalysts with 60 % Pt loading are electrochemically more active than electrodes with a lower Pt loading.
6. Recalculated kinetic current density values taking into account the surface area of the metallic nanoparticles (S_A) are higher for the catalysts with the smaller average particle sizes and have a higher catalytic activity towards ORR.
7. The electroreduction peak potentials (E_p) are shifted towards more positive electrode potentials with increasing of the Pt loading in the catalyst and with the decrease of the average Pt nanoparticle size, if the Pt loading is constant.
8. The capacitance values of the catalyst material (C_{cv}) increase in the following sequence: 60 % Pt–Vulcan, 20 % Pt–Vulcan, 60 % Pt–C(Mo$_2$C)-II, 60 % Pt–C(Mo$_2$C)-I, and 20 % Pt–C(Mo$_2$C).

References

1. K.A. Kuttiyiel, K. Sasaki, Y. Choi, D. Su, P. Liu, R.R. Adzic, Nano Lett. **12**, 6266 (2012)
2. Z.Q. Tian, S.P. Jiang, Y.M. Liang, P.K. Shen, J. Phys. Chem. B **110**, 5343 (2006)
3. J. Perez, E.R. Gonzalez, E.A. Ticianelli, Electrochim. Acta **44**(8–9), 1329 (1998)
4. F. Şen, G. Gökağaç, J. Phys. Chem. C **111**, 5715 (2007)
5. L. Genies, R. Faure, R. Durand, Electrochim. Acta **44**, 1317 (1998)
6. Y.H. Cho, H.S. Park, Y.H. Cho, D.S. Jung, H.Y. Park, Y.E. Sung, J. Power Sources **172**, 89 (2007)
7. J. Prabhuram, T.S. Zhao, C.W. Wong, J.W. Guo, J. Power Sources **134**, 1 (2004)
8. M. Gara, E. Laborda, P. Holdway, A. Crossley, C.J.V. Jones, R.G. Compton, Phys. Chem. Chem. Phys. **15**, 19487 (2013)
9. K. Ward, M. Gara, N.S. Lawrence, R.S. Hartshorne, R.G. Compton, J. Electroanal. Chem. **695**, 1 (2013)
10. J. Masa, C. Batchelor-McAuley, W. Schuhmann, R.G. Compton, Nano Res. **7**(1), 71 (2014)
11. L. Jiang, A. Hsu, D. Chu, R. Chen, J. Electroanal. Chem. **629**, 87 (2009)
12. R. Chen, H. Li, D. Chu, G. Wang, J. Phys. Chem. C **113**, 20689 (2009)
13. L. Genies, Y. Bultel, R. Faure, R. Durand, Electrochim. Acta **48**, 3879 (2003)
14. J. Qiao, L. Xu, L. Ding, P. Shi, L. Zhang, R. Baker, J. Zhang, Int. J. Electrochem. Sci. **8**, 1189 (2013)
15. M. Gara, R.G. Compton, New J. Chem. **35**, 2647 (2011)
16. E. Härk, R. Jäger, E. Lust, ECS Trans. **59**(1), 137 (2014)
17. R. Jäger, E. Härk, P.E. Kasatkin, E. Lust, J. Electrochem. Soc. **161**(9), F861 (2014)
18. I. Morcos, E. Yeager, Electrochim. Acta **15**, 953 (1970)
19. R. Rizo, E. Herrero, J.M. Feliu, Phys. Chem. Chem. Phys. **15**, 15416 (2013)
20. J. Guo, A. Hsu, D. Chu, R. Chen, J. Phys. Chem. C **114**, 4324 (2010)
21. S. Sharma, B.G. Pollet, J. Power Sources **208**, 96 (2012)
22. E. Antolini, E.R. Gonzalez, J. Power Sources **195**, 3431 (2010)
23. E. Yeager, Electrochim. Acta **29**, 1527 (1984)
24. G.S. Chai, S.B. Yoon, J.-S. Yu, J.-H. Choi, Y.-E. Sung, J. Phys. Chem. B **108**, 7074 (2004)
25. T.J. Schmidt, V. Stamenkovic, P.N. Ross Jr., N.M. Markovic, Phys. Chem. Chem. Phys. **5**, 400 (2003)
26. J. Zhang (ed.), *PEM Fuel Cell Electrocatalysts and Catalyst Layers: Fundamentals and Applications* (Springer, London, 2008), pp. 89–134
27. F. Jaouen, J. Phys. Chem. C **113**, 15433 (2009)
28. E. Lust, E. Härk, J. Nerut, K. Vaarmets, Electrochim. Acta **101**, 130 (2013)
29. E. Härk, J. Nerut, K. Vaarmets, I. Tallo, H. Kurig, J. Eskusson, K. Kontturi, E. Lust, J. Electroanal. Chem. **689**, 176 (2013)

30. E. Härk, S. Sepp, P. Valk, K. Vaarmets, J. Nerut, R. Jäger, E. Lust, ECS Trans. **45**(21), 1 (2013)
31. R. Jäger, P.E. Kasatkin, E. Härk, E. Lust, Electrochem. Comm. **35**, 97 (2013)
32. M.P. Hogarth, J. Munk, A.K. Shukla, A.J. Hamnett, J. Appl. Electrochem. **24**, 85 (1994)
33. T.R. Ralph, G.A. Hards, J.E. Keating, S.A. Campbell, D.P. Wilkinson, M. Davis, J. St-Pierre, M.C. Johnson, J. Electrochem. Soc. **144**, 3845 (1997)
34. F. Gloaguen, J.M. Leger, C. Lamy, J. Appl. Electrochem. **27**, 1052 (1997)
35. A. Jänes, T. Thomberg, H. Kurig, E. Lust, Carbon **47**, 23 (2009)
36. G. Álvarez, F. Alcaide, O. Miguel, L. Calvillo, M.J. Lázaro, J.J. Quintana, J.C. Calderón, E. Pastor, I. Esparbé, J. Solid State Electrochem. **14**, 1027 (2010)
37. E. Yeager, J. Mol. Catal. **38**, 5 (1986)
38. K. Kinoshita, *Electrochemical Oxygen Technology* (Wiley, New York, 1992), pp. 5–448
39. R. Adžić in: J. Lipkowski, P.N. Ross (Eds.), Electrocatalysis, Wiley-VCH, New York (1988) 197–242
40. H.A. Gasteiger, S.S. Kocha, B. Sompalli, F.T. Wagner, Appl. Catal. B **56**, 9 (2005)
41. B. Wang, J. Power Sources **152**, 1 (2005)
42. A.J. Bard, L.R. Faulkner, *Electrochemical Methods*, 2nd edn. (Wiley, New York, 2001)
43. R.E. Davis, G.L. Horvath, C.W. Tobias, Electrochim. Acta **12**, 287 (1967)
44. R. Giorgi, P. Ascarelli, V. Contini, S. Turtù, Appl. Surf. Sci. **178**, 149 (2001)
45. NIST X-ray Photoelectron Spectroscopy Database®, NIST Standard Reference Database 20, Version 4.1, http://srdata.nist.gov/xps/
46. S. Brunauer, P.H. Emmett, E. Teller, J. Am. Chem. Soc. **60**, 309 (1938)
47. P.I. Ravikovitch, A.V. Neimark, Colloids. Surf. A: Physicochem. Eng. Aspects **11**, 187–188 (2001)
48. E. Higuchi, H. Uchida, M. Watanabe, J. Electroanal. Chem. **583**, 69 (2005)
49. E. Laviron, J. Electroanal. Chem. **101**, 19 (1979)
50. M. Gara, K.R. Ward, R.G. Compton, Nanoscale **5**, 7304 (2013)